

Environment-Driven Online LiDAR-Camera Extrinsic Calibration

Zhiwei Huang^{ID}, *Graduate Student Member, IEEE*, Jiaqi Li^{ID}, *Student Member, IEEE*,
Ping Zhong^{ID}, *Senior Member, IEEE*, and Rui Fan^{ID}, *Senior Member, IEEE*

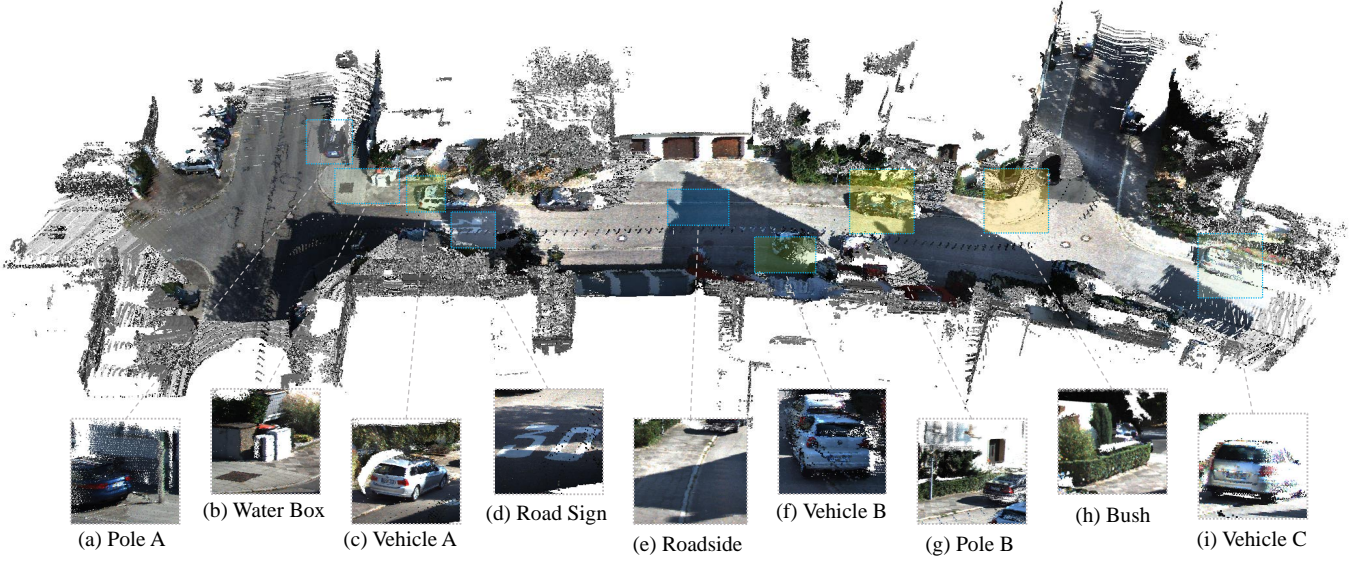


Fig. 1. Visualization of calibration results through LiDAR and camera data fusion in KITTI odometry 00 sequence: (a)-(i) zoomed-in regions that illustrate the alignment between the camera images and the LiDAR point clouds.

Abstract—LiDAR-camera extrinsic calibration (LCEC) is the core for data fusion in computer vision. Existing methods typically rely on customized calibration targets or fixed scene types, lacking the flexibility to handle variations in sensor data and environmental contexts. This paper introduces EdO-LCEC, the first environment-driven, online calibration approach that achieves human-like adaptability. Inspired by the human perceptual system, EdO-LCEC incorporates a generalizable scene discriminator to actively interpret environmental conditions,

creating multiple virtual cameras that capture detailed spatial and textural information. To overcome cross-modal feature matching challenges between LiDAR and camera, we propose dual-path correspondence matching (DPCM), which leverages both structural and textural consistency to achieve reliable 3D-2D correspondences. Our approach formulates the calibration process as a spatial-temporal joint optimization problem, utilizing global constraints from multiple views and scenes to improve accuracy, particularly in sparse or partially overlapping sensor views. Extensive experiments on real-world datasets demonstrate that EdO-LCEC achieves state-of-the-art performance, providing reliable and precise calibration across diverse, challenging environments.

This research was supported by the National Natural Science Foundation of China under Grants 62473288 and 62233013, the Fundamental Research Funds for the Central Universities, Xiaomi Young Talents Program, and the National Key Laboratory of Human-Machine Hybrid Augmented Intelligence, Xi'an Jiaotong University under Grant No. HMHAI-202406. (*Corresponding author: Rui Fan*)

Zhiwei Huang and Jiaqi Li are with the Department of Control Science & Engineering, the College of Electronics & Information Engineering, Tongji University, Shanghai 201804, China (e-mails: {2431985, 2251550}@tongji.edu.cn).

Ping Zhong is with the School of Computer Science and Engineering, Central South University, Changsha 410083, Hunan, China, as well as with the National Key Laboratory of Science and Technology on Automatic Target Recognition, National University of Defense Technology, Changsha 410073, Hunan, China (e-mail: ping.zhong@csu.edu.cn).

Rui Fan is with the Department of Control Science & Engineering, the College of Electronics & Information Engineering, Shanghai Research Institute for Intelligent Autonomous Systems, the State Key Laboratory of Intelligent Autonomous Systems, and Frontiers Science Center for Intelligent Autonomous Systems, Tongji University, Shanghai 201804, China, as well as with the National Key Laboratory of Human-Machine Hybrid Augmented Intelligence, Institute of Artificial Intelligence and Robotics, Xi'an Jiaotong University, Xi'an 710049, Shaanxi, China (e-mail: rui.fan@ieec.org).

I. INTRODUCTION

We have long envisioned robots with human-like intelligence, enabling them to understand, adapt to, and positively impact the world [1]–[4]. This dream is becoming increasingly attainable with the advent of LiDAR-camera data fusion systems. LiDARs provide accurate spatial information, while cameras capture rich textural details [5]. The complementary strengths of these two modalities, when fused, provide robots with powerful environmental perception capabilities [6], [7]. LiDAR-camera extrinsic calibration (LCEC), which estimates the rigid transformation between the two sensors, is a core and foundational process for effective data fusion.

Current LiDAR-camera extrinsic calibration methods are primarily categorized as either target-based or target-free. Target-based approaches [8]–[13] have long been the preferred choice in this field. They are typically offline, relying on customized calibration targets (typically checkerboards). However, they often demonstrate poor adaptability to real-world environments. This is largely because extrinsic parameters may change significantly due to moderate shocks or during extended operations in environments with vibrations. Online, target-free approaches aim at overcoming this problem by extracting informative visual features directly from the environment. Previous works [14], [15] estimate the extrinsic parameters by matching the cross-modal edges between LiDAR projections and camera images. While effective in specific scenarios with abundant features, these traditional methods heavily rely on well-distributed edge features. Recent advances in deep learning techniques have spurred extensive explorations, such as [16] and [5], to leverage semantic information to aid cross-modal feature matching. Although these approaches have shown compelling performance in specific scenarios, such as parking lots, they predominantly rely on curated, pre-defined objects, *e.g.*, vehicles [17], lanes [16], poles [18], and stop signs [19]. On the other hand, several end-to-end deep learning networks [20]–[25] have been developed to find a more direct solution for LCEC. While these methods have demonstrated effectiveness on large-scale datasets like KITTI [26], they suffer from a high dependency on the training setup and are thus less generalizable. Overall, existing methods passively rely on predefined techniques to identify certain preset scene features. They lack the flexibility needed to adapt and respond effectively to environmental changes. In contrast, human actions are environment-driven. People intuitively assess their surroundings, swiftly respond to changes, make adaptive decisions, and improve through interaction and feedback. Elevating online calibration to this level of human-like adaptability presents a compelling research direction.

In this work, we take one step forward in the field of online LCEC by designing an environment-driven framework EdO-LCEC. As illustrated in Fig. 1, our approach treats sensors’ operational environment as a spatial-temporal flow. By selectively combining information from multiple scenes across different times, this approach could achieve high-precision calibration dynamically. A prerequisite for the success of EdO-LCEC is the design of a generalizable scene discriminator. The scene discriminator employs large vision models to conduct depth estimation and image segmentation, achieving high-quality environmental perception on semantic and spatial dimensions. In detail, it calculates the feature density of the calibration scene and uses this information to guide the generation of multiple virtual cameras for projecting LiDAR intensities and depth. This improved LiDAR point cloud projecting strategy increases the available environmental features, and thus overcomes the previous reliance of algorithms [14], [27] on uniformly distributed geometric or textural features. At each scene, we perform dual-path correspondence matching (DPCM). Drawing inspiration from the human visual system [28], DPCM divides correspondence matching into spatial and textural pathways to fully leverage both geometric

and semantic information. Each pathway constructs a cost matrix based on structural and textural consistency, guided by accurate semantic priors, to yield reliable 3D-2D correspondences. Finally, the correspondences obtained from multiple views and scenes are used as inputs for our proposed spatial-temporal relative pose optimization, which derives and refines the extrinsic matrix between LiDAR and camera. Through extensive experiments conducted on three real-world datasets, EdO-LCEC demonstrates superior robustness and accuracy compared to other SoTA online, target-free approaches.

To summarize, our novel contributions are as follows:

- EdO-LCEC, the first environment-driven, online LCEC framework that achieves high calibration accuracy and human-like adaptability.
- Generalizable scene discriminator, which can automatically perceive the calibration scene and capture potential spatial, textural and semantic features using SoTA LVMs.
- DPCM, a novel cross-modal feature matching algorithm consisting of textural and spatial pathways, capable of generating dense and reliable 3D-2D correspondences between LiDAR point cloud and camera image.
- Spatial-temporal relative pose optimization, enabling high-quality extrinsic estimation through multi-view and multi-scene optimization.

II. RELATED WORK

Target-based methods achieve high accuracy using customized calibration targets (typically checkerboards). However, they require offline execution and are significantly limited in dynamic or unstructured environments where such targets are unavailable [29], [30]. Recent studies have shifted to online, target-free methods to overcome these limitations. Pioneering works [14], [15], [31]–[34] estimate the relative pose between the two sensors by aligning the cross-modal edges or mutual information (MI) extracted from LiDAR projections and camera RGB images. While effective in specific scenarios with abundant features, these traditional methods heavily rely on well-distributed edges and rich texture, which largely compromise calibration robustness. To circumvent the challenges associated with cross-modal feature matching, several studies [29], [35]–[37] have explored motion-based methods. These approaches match sensor motion trajectories from visual and LiDAR odometry to derive extrinsic parameters through optimization. While they effectively accommodate heterogeneous sensors without requiring overlap, they demand precise synchronized LiDAR point clouds and camera images to accurately estimate per-sensor motion, which limits their applicability.

Advances in deep learning techniques have driven significant exploration into enhancing traditional target-free algorithms. Some studies [5], [16]–[19], [27], [30], [38] explore attaching deep learning modules to their calibration framework as useful tools to enhance calibration efficiency. For instance, [16] accomplishes LiDAR and camera registration by aligning road lanes and poles detected by semantic segmentation. Similarly, [19] employs stop signs as calibration primitives and refines results over time using a Kalman filter. A recent study

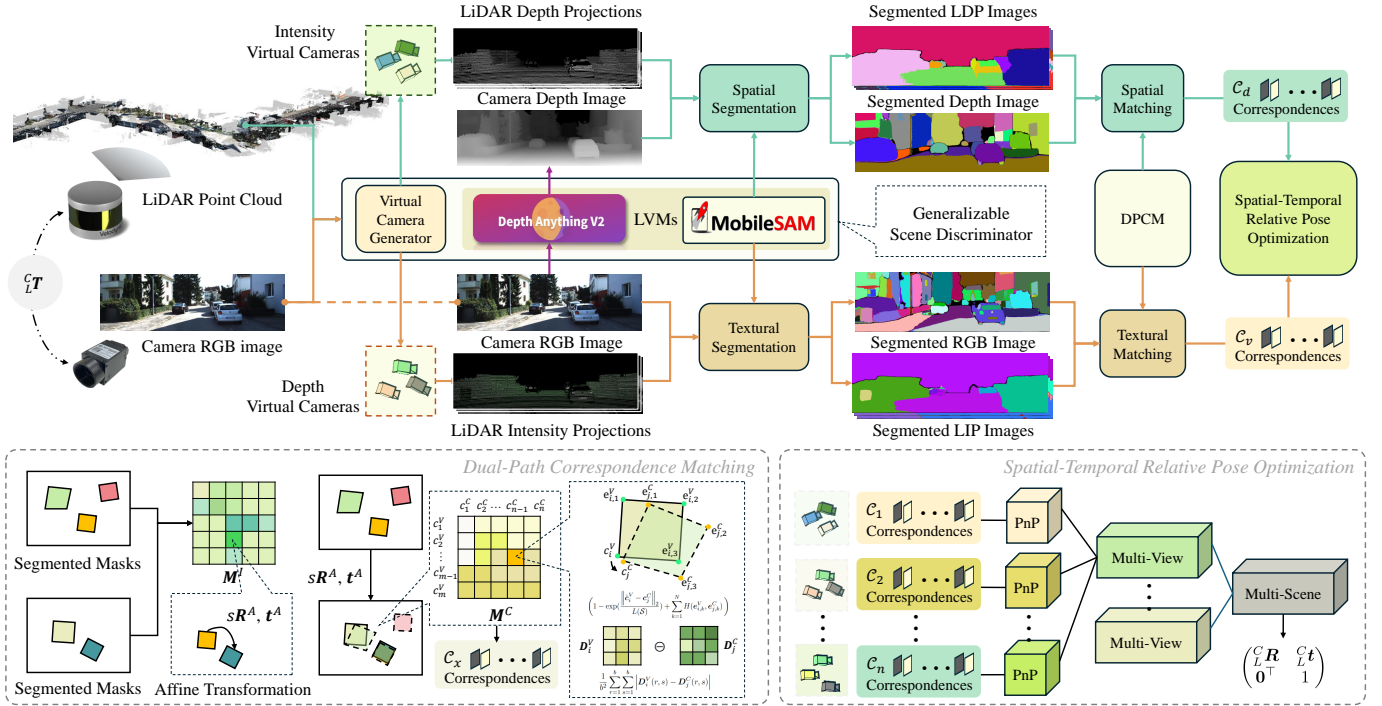


Fig. 2. The pipeline of our proposed EdO-LCEC. We use the generalizable scene discriminator to calculate the feature density of each calibration scene by image segmentation and depth estimation. Based on this feature density, the scene discriminator generates multiple depth and intensity virtual cameras to create LIP and LDP images. Image segmentation results of virtual images and camera images are sent to the dual-path correspondence matching module to obtain dense 3D-2D correspondences, which serve as input for the spatial-temporal relative pose optimization to derive and refine the extrinsic matrix between LiDAR and camera from multiple views and scenes.

[27] introduced Direct Visual LiDAR Calibration (DVL), a novel point-based method that utilizes SuperGlue [39] to establish direct 3D-2D correspondences between LiDAR and camera data. On the other hand, several learning-based algorithms [20]–[25] try to covert calibration process into more direct approaches by exploiting end-to-end deep learning networks. Although these methods have demonstrated effectiveness on public datasets like KITTI [26], which primarily focuses on urban driving scenarios, their performance has not been extensively validated on other types of real-world datasets that contain more challenging scenes. Furthermore, their dependence on pre-defined sensor configurations (both LiDAR and camera) poses implementation challenges. In comparison, our approach actively perceives the environment and achieves human-like adaptability. This environment-driven strategy enables robots to rapidly obtain high-precision extrinsic parameters anytime and anywhere.

III. METHODOLOGY

Given LiDAR point clouds and camera images, our goal is to estimate their extrinsic matrix ${}^C_L \mathbf{T}$, defined as follows:

$${}^C_L \mathbf{T} = \begin{bmatrix} {}^C_L \mathbf{R} & {}^C_L \mathbf{t} \\ \mathbf{0}^\top & 1 \end{bmatrix} \in SE(3), \quad (1)$$

where ${}^C_L \mathbf{R} \in SO(3)$ represents the rotation matrix, ${}^C_L \mathbf{t}$ denotes the translation vector, and $\mathbf{0}$ represents a column vector of zeros. We first give an overview of the proposed method, as shown in Fig. 2. It mainly contains three stages:

- We first utilize a scene discriminator to understand the environment through image segmentation and depth estimation, generating virtual cameras that project LiDAR intensity and depth from multiple viewpoints (Sect. III-A).
- The image segmentation outputs are processed along two pathways (spatial and textural), then input into a dual-path correspondence matching module to establish reliable 3D-2D correspondences (Sect. III-B).
- The obtained correspondences are used as inputs for our proposed spatial-temporal relative pose optimization, which derives and refines the extrinsic matrix (Sect. III-C).

A. Generalizable Scene Discriminator

Our environment-driven approach first employs a generalizable scene discriminator to interpret the surroundings by generating virtual cameras to project LiDAR point cloud intensities and depth. This discriminator configures both an intensity and a depth virtual camera from the LiDAR’s perspective. This setup yields a LiDAR intensity projection (LIP) image ${}^V_I \mathbf{I} \in \mathbb{R}^{H \times W \times 1}$ (H and W represent the image height and width) and a LiDAR depth projection (LDP) image ${}^V_D \mathbf{I}$. To align with the LDP image, the input camera RGB image ${}^C_I \mathbf{I}$ is processed using Depth Anything V2 [40] to obtain estimated depth images ${}^C_D \mathbf{I}^1$. To take advantage of semantic information,

¹In this article, the symbols in the superscript denote the type of target camera (V denotes virtual camera and C indicates real camera), and the subscript denotes the source of the image (D is depth and I is intensity).

we utilize MobileSAM [41] as the image segmentation backbone. The series of n detected masks in an image is defined as $\{\mathcal{M}_1, \dots, \mathcal{M}_n\}$. The corner points along the contours of masks detected are represented by $\{c_1, \dots, c_{m_i}\}$, where m_i is the total corner points number in the i -th mask. An instance (bounding box), utilized to precisely fit around each mask, is centrally positioned at \mathbf{o} and has a dimension of $h \times w$ pixels. We define the corresponding depth of a corner point as d , and $\mathbf{D} \in \mathbb{R}^{b \times b}$ as the matrix that stores texture values in its b -neighborhood. To fully leverage the structured information within the masks, we construct a convex polygon from the corner points. As depicted in Fig. 2, the neighboring vertices of a corner point c_i is defined as $\{e_{i,1}, \dots, e_{i,k}\}$.

For each virtual or camera image \mathbf{I} , the scene discriminator computes its feature density $\rho(\mathbf{I})$, providing critical cues for feature extraction and correspondence matching. The feature density $\rho(\mathbf{I})$ is defined as follows:

$$\rho(\mathbf{I}) = \underbrace{\left(\frac{1}{n} \log \sum_{i=1}^n \frac{m_i}{|\mathcal{M}_i|} \right)}_{\rho_t} \underbrace{\left(\sum_{i=1}^n \log \frac{|\bigcap_{j=1}^n \mathcal{M}_j|}{|\mathcal{M}_i|} \right)}_{\rho_s}, \quad (2)$$

where ρ_t denotes the textural density and ρ_s represents the structural density. The occlusion challenges caused by the different perspectives of LiDAR and the camera [5], [14], combined with limited feature availability in sparse point clouds, mean that a single pair of virtual cameras is insufficient for a comprehensive view of the calibration scene. Let E represent the event of capturing enough effective features, with probability $P(E) = \lambda$. If we have n_I intensity virtual cameras and n_D depth virtual cameras, the probability of capturing enough effective features is $1 - (1 - \lambda)^{n_I + n_D}$. In theory, as $n_I + n_D \rightarrow \infty$, the probability $P(E)^{n_I + n_D} \rightarrow 0$, leading to $1 - (1 - \lambda)^{n_I + n_D} \rightarrow 1$. Increasing the number of virtual cameras raises the likelihood of capturing more potential correspondences, thus enhancing calibration accuracy. However, applying an infinite number of virtual cameras during calibration is impractical. Considering the trade-off between calibration accuracy and compute resources, we set the number of multiple virtual cameras to satisfy the balance of feature density:

$$\rho(\mathcal{I}^C) + \rho(\mathcal{D}^C) = \sum_{i=0}^{n_I} \rho(\mathcal{I}_i^V) + \sum_{i=0}^{n_D} \rho(\mathcal{D}_i^V). \quad (3)$$

In practical applications, we set multiple virtual cameras inside a sphere originating from the LiDAR perspective center. Since the feature density is similar if the perspective viewpoints of virtual cameras are close to the initial position, we can assume that $\rho(\mathcal{I}_i^V) \approx \rho(\mathcal{I}_0^V)$ and $\rho(\mathcal{D}_i^V) \approx \rho(\mathcal{D}_0^V)$. So n_I and n_D can be obtained as follows:

$$n_I = \frac{\rho(\mathcal{I}^C)}{\rho(\mathcal{I}_0^V)}, \quad n_D = \frac{\rho(\mathcal{D}^C)}{\rho(\mathcal{D}_0^V)}. \quad (4)$$

Once all virtual cameras are generated, the discriminator performs image segmentation on each LiDAR projection captured from multiple views, detecting the corner points of the masks. These masks with detected corner points serve as inputs for the dual-path correspondence matching.

B. Dual-Path Correspondence Matching

Given the segmented masks and detected corner points, dual-path correspondence matching leverages them to achieve dense and reliable 3D-2D correspondences. Inspired by human visual system, DPCM consists of two pathways, one for correspondence matching of LIP and RGB images, and the other for LDP and depth images. For each pathway, DPCM adopted the approach outlined in [5] to obtain mask matching result $\mathcal{A} = \{(\mathcal{M}_i^V, \mathcal{M}_i^C) \mid i = 1, \dots, m\}$ from a cost matrix \mathbf{M}^I . Each matched mask pair can estimate an affine transformation $[s\mathbf{R}^A, \mathbf{t}^A] \in SE(2)$ to guide the correspondence matching. Specifically, we update the corner points c_i^V in the virtual image to a location \hat{c}_i^V that is close to its true projection coordinate using this affine transformation, as follows:

$$\hat{c}_i^V = s\mathbf{R}^A(c_i^V) + \mathbf{t}^A. \quad (5)$$

To determine optimum corner point matches, we construct a cost matrix \mathbf{M}^C , where the element at $\mathbf{x} = [i, j]^T$, namely:

$$\begin{aligned} \mathbf{M}^C(\mathbf{x}) = & \underbrace{\rho_s \left(1 - \exp\left(\frac{\|\hat{c}_i^V - c_j^C\|^2}{L(\mathcal{A})}\right) + \sum_{k=1}^N H(e_{i,k}^V, e_{j,k}^C) \right)}_{\text{Structural Consistency}} \\ & + \underbrace{\rho_t \left(\frac{1}{b^2} \sum_{r=1}^b \sum_{s=1}^b |D_i^V(r, s) - D_j^C(r, s)| \right)}_{\text{Textural Consistency}} \end{aligned} \quad (6)$$

denotes the matching cost between the i -th corner point of a mask in the LiDAR virtual image and the j -th corner point of a mask in the camera image. (6) consists of structural and textural consistency. The structural consistency measures the structural difference of corner points in the virtual and real image, where $L(\mathcal{A})$ denotes the average perimeter of the matched masks and $H(e_{i,k}^V, e_{j,k}^C)$ represents the similarity of the neighboring vertices between current and target corner point. The textural consistency derives the relative textural similarity of the b neighboring zone. After establishing the cost matrix, a strict criterion is applied to achieve reliable matching. Matches with the lowest costs in both horizontal and vertical directions of $\mathbf{M}^C(\mathbf{x})$ are determined as the optimum corner point matches. Since every c_i^V can trace back to a LiDAR 3D point $\mathbf{p}_i^L = [x^L, y^L, z^L]^T$, and every c_i^C is related to a pixel $\mathbf{p}_i = [u, v]^T$ (represented in homogeneous coordinates as $\tilde{\mathbf{p}}_i$) in the camera image, the final correspondence matching result of DPCM is $\mathcal{C} = \{(\mathbf{p}_i^L, \mathbf{p}_i) \mid i = 1, \dots, q\}$.

C. Spatial-Temporal Relative Pose Optimization

EdO-LCEC treats the sensor's operational environment as a spatial-temporal flow composed of N multiple scenes across different time instances. In situations with incomplete or sparse point clouds, single-view methods such as [5], [14] are constrained by the limited number of high-quality correspondences. Our environment-driven approach addresses this limitation by integrating multi-view and multi-scene optimization. By merging the optimal matching results from multiple

time instances and scenes, this spatial-temporal optimization enhances the selection of correspondences, maximizing the number of high-quality matches and ultimately improving overall calibration accuracy.

Multi-View Optimization. In multi-view optimization, the extrinsic matrix ${}^C_L\hat{\mathbf{T}}_t$ of the t -th scene can be formulated as follows:

$${}^C_L\hat{\mathbf{T}}_t = \arg \min \sum_{{}^C_L\mathbf{T}_{t,k}} \sum_{i=1}^{n_I+n_D} \sum_{(\mathbf{p}_i^L, \mathbf{p}_j) \in \mathcal{C}_i} G \left(\underbrace{\|\pi({}^C_L\mathbf{T}_{t,k}\mathbf{p}_j^L) - \tilde{\mathbf{p}}_j\|_2}_{\epsilon_j} \right), \quad (7)$$

where ${}^C_L\mathbf{T}_{t,k}$ denotes the k -th PnP solution obtained using a selected subset \mathcal{V}_k of correspondences from \mathcal{C}_i , and ϵ_j represents the reprojection error of $(\mathbf{p}_i^L, \mathbf{p}_j)$ with respect to ${}^C_L\mathbf{T}_{t,k}$. $G(\epsilon_j)$ represents the gaussian depth-normalized reprojection error under the projection model π , defined as:

$$G(\epsilon_j) = \frac{\epsilon_j(e - \mathcal{K}(d'_j, \bar{d}'))}{H + \epsilon_j}, \quad (8)$$

where d'_j is the normalized depth of \mathbf{p}_j^L , \bar{d}' is the average normalized depth, and $\mathcal{K}(d'_j, \bar{d}')$ is a gaussian kernel.

Multi-Scene Optimization. In each scenario, we choose a reliable subset \mathcal{S}_t , which can be obtained as follows:

$$\mathcal{S}_t = \bigcap_{k=1}^{s_t} \mathcal{V}_{t,k}, \quad s_t = \min \left\{ \frac{Q_{\max} q_t}{\sum_{j=1}^N q_j}, s_{\max} \right\}, \quad (9)$$

where $\mathcal{V}_{t,k}$ is the correspondence subset in the t -th scene with the k -th smallest mean reprojection error under its PnP solution. q_t denotes the number of correspondences in the t -th scene. Q_{\max} and s_{\max} represent the maximum number of subsets across all scenarios and the maximum number of reliable subsets in a single scene, respectively. The multi-scene optimization process then solves the final extrinsic matrix ${}^C_L\mathbf{T}^*$ by minimizing the joint reprojection error:

$$\mathcal{L}({}^C_L\mathbf{T}^*) = \sum_{t=1}^N \sum_{(\mathbf{p}_i^L, \mathbf{p}_j) \in \mathcal{S}_t} G \left(\|\pi({}^C_L\mathbf{T}^*\mathbf{p}_j^L) - \tilde{\mathbf{p}}_j\|_2 \right) \quad (10)$$

across multiple spaces in the environment at different times. This process effectively combines optimal correspondences from both spatial and textural pathways in each scenario, enabling environment-driven spatial-temporal optimization and achieving human-like adaptability to the environment.

IV. EXPERIMENT

A. Experimental Setup and Evaluation Metrics

In our experiments, we compare our proposed EdO-LCEC with SoTA online, target-free LCEC approaches on the public dataset KITTI odometry [26] (including 00-09 sequences) and MIAS-LCEC [5] (including target-free datasets MIAS-LCEC-TF70 and MIAS-LCEC-TF360). To comprehensively evaluate calibration accuracy, we quantify LCEC performance using the Euler angle error magnitude e_r and the translation error magnitude e_t .

Notably, sequences in KITTI odometry, aside from 00, were included in the training datasets for the learning-based methods [20], [21], [23], [25]. To ensure a fair comparison,

we reproduced calibration results for both the left and right cameras on sequence 00 when the authors provided their code; otherwise, we used the reported results for the left camera from their papers. Since most learning-based methods lack APIs for custom data, our comparison with these methods is limited to the KITTI odometry 00 sequence. For experiments on the MIAS-LCEC dataset, as the results for the compared methods [5], [14]–[16], [27] are reported in [5], we directly use the values presented in that paper.

B. Comparison with State-of-the-Art Method

In this section, quantitative comparisons with SoTA approaches on three datasets are presented in Fig. 6, Tables I, II, III, and IV. Additionally, qualitative results are illustrated in Figs. 5 and 4.

Evaluation on KITTI odometry. The results shown in Table I and II suggest that, with the exception of sequences 01 and 04, our method achieves SoTA performance across the ten sequences (00-09) in KITTI odometry. Specifically, in the 00 sequence, EdO-LCEC reduces the e_r by around 35.2-99.8% and the e_t by 11.8-98.7% for the left camera, and reduces the e_r by around 46.9-99.7% and the e_t by 13.9-97.6% for the right camera. Additionally, according to Fig. 4, it can be observed that the point cloud of a single frame in KITTI is so sparse that the other approaches behave poorly. In contrast, our proposed method overcomes this difficulty and achieves high-quality data fusion through the calibration result. We attribute these performance improvements to our spatial-temporal relative pose optimization. Merging the optimal matching results from multiple views and scenes maximizes the number of reliable correspondences and ultimately improves overall calibration accuracy.

Evaluation on MIAS-LCEC Dataset. Compared to the sparse point clouds in the KITTI dataset, the point clouds in the MIAS-LCEC datasets are significantly denser, which facilitates feature matching and allows us to test the upper limits of the algorithm calibration accuracy. The results shown in Table III demonstrate that our method outperforms all other SoTA approaches on MIAS-LCEC-TF70. It can also be observed that our method dramatically outperforms CRLF, UMich, DVL, HKU-Mars, and is slightly better than MIAS-LCEC across the total six subsets. In challenging conditions that are under poor illumination and adverse weather, or when few geometric features are detectable, EdO-LCEC performs significantly better than all methods, particularly. This impressive performance can be attributed to the generalizable scene discriminator. The multiple virtual cameras generated by the scene discriminator provide a comprehensive perception of the calibration scene from both spatial and textural perspectives, which largely increases the possibility of capturing high-quality correspondences for the PnP solver. Furthermore, the data fusion results in Fig. 5, obtained using our optimized extrinsic matrix, visually demonstrate perfect alignment on the checkerboard. This highlights the high calibration accuracy achieved by our method.

²The results generated by LCCNet using the authors' code yield higher errors compared to those reported in their paper.

TABLE I

QUANTITATIVE COMPARISONS WITH SoTA TARGET-FREE LCEC APPROACHES ON THE 00 SEQUENCE OF KITTI ODOMETRY. THE BEST RESULTS ARE SHOWN IN BOLD TYPE. †: THESE METHODS DID NOT RELEASE (ENGLISH-SPEAKING) CODE PREVENTING REPRODUCING RESULTS FOR BOTH CAMERAS.

Approach	Initial Range	Left Camera						Right Camera									
		Magnitude		Rotation Error ($^{\circ}$)			Translation Error (m)			Magnitude		Rotation Error ($^{\circ}$)			Translation Error (m)		
		e_r ($^{\circ}$)	e_t (m)	Yaw	Pitch	Roll	X	Y	Z	e_r ($^{\circ}$)	e_t (m)	Yaw	Pitch	Roll	X	Y	Z
CalibRCNN [†] [22]	$\pm 10^{\circ} / \pm 0.25m$	0.805	0.093	0.446	0.640	0.199	0.062	0.043	0.054	-	-	-	-	-	-	-	-
CalibDNN [†] [23]	$\pm 10^{\circ} / \pm 0.25m$	1.021	0.115	0.200	0.990	0.150	0.055	0.032	0.096	-	-	-	-	-	-	-	-
RegNet [†] [42]	$\pm 20^{\circ} / \pm 1.5m$	0.500	0.108	0.240	0.250	0.360	0.070	0.070	0.040	-	-	-	-	-	-	-	-
Borer <i>et al.</i> [†] [20]	$\pm 1^{\circ} / \pm 0.25m$	0.455	0.095	0.100	0.440	0.060	0.037	0.030	0.082	-	-	-	-	-	-	-	-
LCCNet [21]	$\pm 10^{\circ} / \pm 1.0m$	1.418	0.600	0.455	0.835	0.768	0.237	0.333	0.329	1.556	0.718	0.457	1.023	0.763	0.416	0.333	0.337
RGGNet [25]	$\pm 20^{\circ} / \pm 0.3m$	1.29	0.114	0.640	0.740	0.350	0.081	0.028	0.040	3.870	0.235	1.480	3.380	0.510	0.180	0.056	0.061
CalibNet [24]	$\pm 10^{\circ} / \pm 0.2m$	5.842	0.140	2.873	2.874	3.185	0.065	0.064	0.083	5.771	0.137	2.877	2.823	3.144	0.063	0.062	0.082
CRLF [16]	-	0.629	4.118	0.033	0.464	0.416	3.648	1.483	0.550	0.633	4.606	0.039	0.458	0.424	4.055	1.636	0.644
UMich [15]	-	4.161	0.321	0.113	3.111	2.138	0.286	0.077	0.086	4.285	0.329	0.108	3.277	2.088	0.290	0.085	0.090
HKU-Mars [14]	-	33.84	6.355	19.89	18.71	19.32	3.353	3.232	2.419	32.89	4.913	18.99	15.77	17.00	2.917	2.564	1.646
DVL [27]	-	122.1	5.129	48.64	87.29	98.15	2.832	2.920	1.881	120.5	4.357	49.60	87.99	96.72	2.086	2.517	1.816
MIAS-LCEC [5]	-	5.385	1.014	1.574	4.029	4.338	0.724	0.383	0.343	7.655	1.342	1.910	5.666	6.154	0.843	0.730	0.358
EdO-LCEC (Ours)	-	0.295	0.082	0.117	0.176	0.150	0.051	0.044	0.032	0.336	0.118	0.216	0.168	0.121	0.083	0.067	0.032

TABLE II

COMPARISONS WITH SoTA LCEC APPROACHES ON KITTI ODOMETRY (01-09 SEQUENCES). THE BEST RESULTS ARE SHOWN IN BOLD TYPE.

Approach	01		02		03		04		05		06		07		08		09	
	e_r	e_t																
CRLF [16]	0.623	7.363	0.632	3.642	0.845	6.007	0.601	0.372	0.616	5.961	0.615	25.762	0.606	1.807	0.625	5.376	0.626	5.133
UMich [15]	2.196	0.305	3.733	0.331	3.201	0.316	2.086	0.348	3.526	0.356	2.914	0.353	3.928	0.368	3.722	0.367	3.117	0.363
HKU-Mars [14]	20.73	3.770	32.95	12.70	21.99	3.493	4.943	0.965	34.42	6.505	25.20	7.437	33.10	7.339	26.62	8.767	20.38	3.459
DVL [27]	112.0	2.514	120.6	4.285	124.7	4.711	113.5	4.871	123.9	4.286	128.9	5.408	124.7	5.279	126.2	4.461	116.7	3.931
MIAS-LCEC [5]	0.621	0.300	0.801	0.327	1.140	0.324	0.816	0.369	4.768	0.775	2.685	0.534	11.80	1.344	5.220	0.806	0.998	0.432
EdO-LCEC (Ours)	2.269	0.459	0.561	0.142	0.737	0.137	1.104	0.339	0.280	0.093	0.485	0.124	0.188	0.076	0.352	0.115	0.386	0.120

TABLE III

COMPARISONS WITH SoTA TARGET-FREE LCEC APPROACHES ON MIAS-LCEC-TF70. THE BEST RESULTS ARE SHOWN IN BOLD TYPE.

Approach	Residential Community		Urban Freeway		Building		Challenging Weather		Indoor		Challenging Illumination		All	
	e_r ($^{\circ}$)	e_t (m)	e_r ($^{\circ}$)	e_t (m)	e_r ($^{\circ}$)	e_t (m)	e_r ($^{\circ}$)	e_t (m)	e_r ($^{\circ}$)	e_t (m)	e_r ($^{\circ}$)	e_t (m)	e_r ($^{\circ}$)	e_t (m)
CRLF [16]	1.594	0.464	1.582	0.140	1.499	20.17	1.646	2.055	1.886	30.05	1.876	19.047	1.683	11.133
UMich [15]	4.829	0.387	2.267	0.166	11.914	0.781	1.851	0.310	2.029	0.109	5.012	0.330	4.265	0.333
HKU-Mars [14]	2.695	1.208	2.399	1.956	1.814	0.706	2.578	1.086	2.527	0.246	14.996	3.386	3.941	1.261
DVL [27]	0.193	0.063	0.298	0.124	0.200	0.087	0.181	0.052	0.391	0.030	1.747	0.377	0.423	0.100
MIAS-LCEC [5]	0.190	0.050	0.291	0.111	0.198	0.072	0.177	0.046	0.363	0.024	0.749	0.118	0.298	0.061
EdO-LCEC (Ours)	0.168	0.044	0.293	0.105	0.184	0.057	0.183	0.044	0.338	0.027	0.474	0.104	0.255	0.055

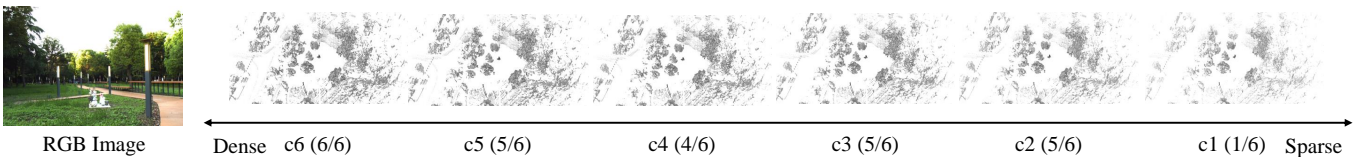


Fig. 3. We divided each point cloud into six equal parts and combined these segments to create point clouds with varying densities.

Additionally, experimental results on the MIAS-LCEC-TF360 further prove our outstanding performance. From Table IV, it is evident that while the other approaches achieve poor performances, our method demonstrates excellent accuracy, indicating strong adaptability to more challenging scenarios, with narrow overlapping areas between LiDAR projections and camera images. This impressive performance can be attributed to our proposed DPCM, a powerful cross-modal feature matching algorithm. DPCM utilizes structural and textural consistency

to jointly constrain correspondences matching on both spatial and textural pathways. This largely increases reliable correspondences compared to DVL and MIAS-LCEC, thereby providing a more reliable foundation for extrinsic parameter optimization.

To evaluate the algorithm's adaptability to incomplete and sparse point clouds, we further segmented the already limited field-of-view point clouds from the MIAS-LCEC-TF360 dataset. Specifically, as shown in Fig. 3, we divided each

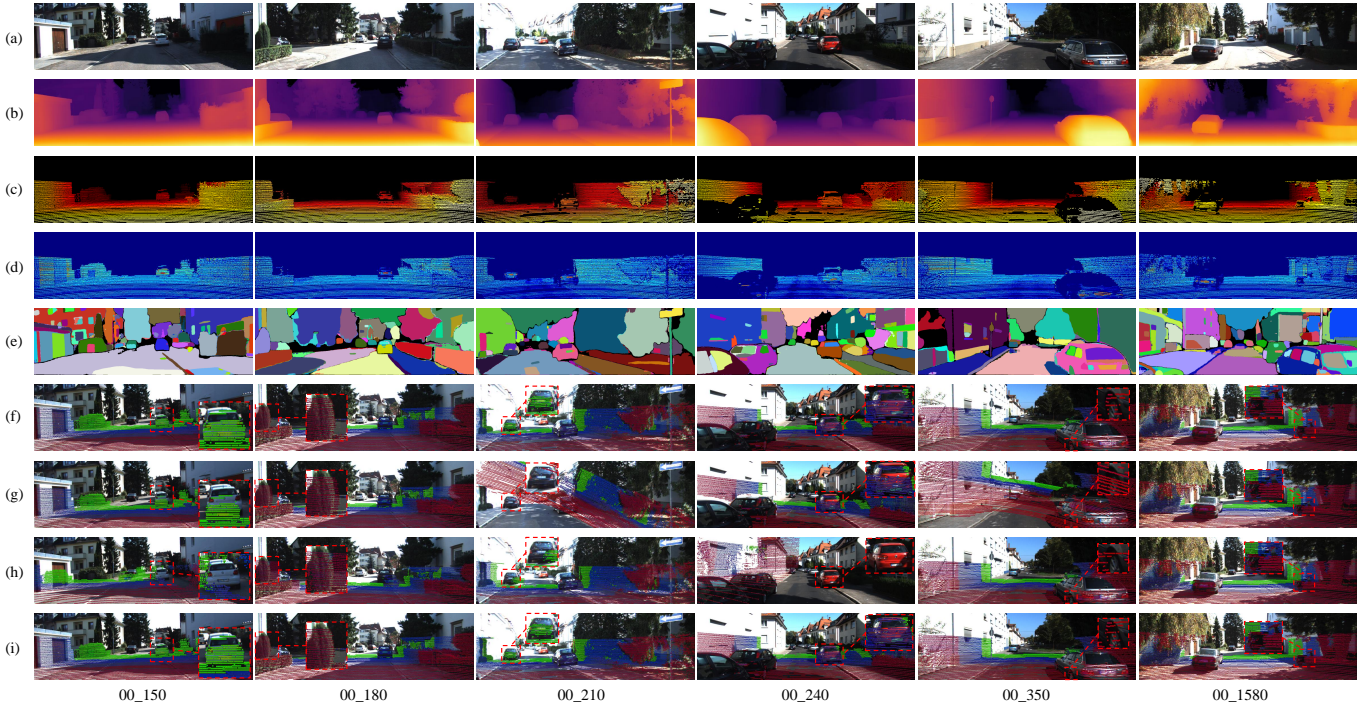


Fig. 4. Qualitative comparisons with SoTA target-free LCEC approaches on the KITTI odometry dataset: (a)-(e) RGB images, Depth images, LDP images, LIP images and image segmentation results; (f)-(i) experimental results achieved using ground truth, UMich, HKU-Mars and EdO-LCEC (ours), shown by merging LiDAR depth projections and RGB images, where significantly improved regions are shown with red dashed boxes.

TABLE IV
QUANTITATIVE COMPARISONS OF OUR PROPOSED EdO-LCEC APPROACH WITH OTHER SoTA TARGET-FREE APPROACHES ON THE MIAS-LCEC-TF360. THE BEST RESULTS ARE SHOWN IN BOLD TYPE.

Approach	Indoor		Outdoor	
	e_r ($^\circ$)	e_t (m)	e_r ($^\circ$)	e_t (m)
CRLF [16]	1.479	13.241	1.442	0.139
UMich [15]	1.510	0.221	6.522	0.269
HKU-Mars [14]	85.834	7.342	35.383	8.542
DVL [27]	39.474	0.933	65.571	1.605
MIAS-LCEC [5]	0.996	0.182	0.659	0.114
EdO-LCEC (Ours)	0.720	0.106	0.349	0.109

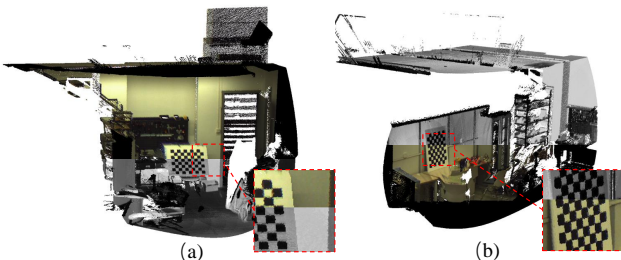


Fig. 5. Visualization of EdO-LCEC calibration results through LiDAR and camera data fusion: (a)-(b) illustrate two LiDAR point clouds in MIAS-LCEC-TF70, partially rendered by color using the estimated extrinsic matrix of EdO-LCEC.

point cloud into six equal parts. By progressively combining these segments, we create point clouds with varying densities, ranging from 1/6 (c1) to the full 6/6 (c6) density.

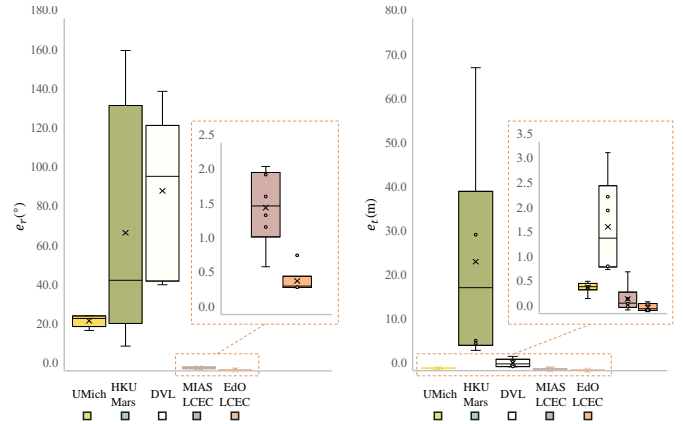


Fig. 6. Comparisons with SoTA approaches on the segmented point clouds from MIAS-LCEC-TF360. The zoomed-in region highlights the comparative details between the algorithms with higher accuracy. Since the results of CRLF are invalid, they were not included in the comparison.

The calibration results presented in Fig. 6 show that EdO-LCEC achieves the smallest mean e_r and e_t , along with the narrowest interquartile range, compared to other approaches across different point cloud densities. This demonstrates the stability and adaptability of EdO-LCEC under challenging conditions involving sparse or incomplete point clouds.

C. Ablation Study and Analysis

To explore the contribution of scene discriminator and spatial-temporal relative pose optimization, we evaluate our algorithm's performance with and without multi-view (includ-

TABLE V
ABLATION STUDY OF DIFFERENT COMPONENTS ON THE 00 SEQUENCE OF KITTI ODOMETRY. THE BEST RESULTS ARE SHOWN IN BOLD TYPE.

Components		Left Camera						Right Camera										
Multi-View		Multi Scene	Magnitude		Rotation Error ($^{\circ}$)			Translation Error (m)			Magnitude		Rotation Error ($^{\circ}$)			Translation Error (m)		
Intensity	Depth		e_r ($^{\circ}$)	e_t (m)	Yaw	Pitch	Roll	X	Y	Z	e_r ($^{\circ}$)	e_t (m)	Yaw	Pitch	Roll	X	Y	Z
			1.625	0.459	0.820	0.669	0.899	0.247	0.235	0.211	1.620	0.472	0.915	0.691	0.807	0.257	0.254	0.197
✓			1.387	0.358	0.755	0.579	0.711	0.189	0.208	0.153	1.641	0.459	1.012	0.679	0.738	0.257	0.257	0.178
✓	✓		1.125	0.280	0.534	0.534	0.613	0.134	0.151	0.136	1.425	0.354	0.856	0.563	0.679	0.186	0.205	0.138
		✓	0.406	0.155	0.180	0.201	0.223	0.119	0.067	0.049	0.447	0.192	0.227	0.243	0.211	0.148	0.094	0.051
✓		✓	0.339	0.110	0.179	0.167	0.162	0.069	0.063	0.039	0.480	0.138	0.322	0.239	0.150	0.096	0.084	0.033
✓	✓	✓	0.295	0.082	0.117	0.176	0.150	0.051	0.044	0.032	0.336	0.118	0.216	0.168	0.121	0.083	0.067	0.032

ing both textural and spatial perspective views) and multi-scene optimizations on the 00 sequence of KITTI odometry. The results presented in Table V demonstrate that lacking any of these components significantly degrades calibration performance. In particular, calibration errors increase substantially when only single-view calibration is applied, as it lacks the comprehensive constraints provided by multi-view inputs. Additionally, the joint optimization from multiple scenes significantly improved the calibration accuracy compared to those only under multi-view optimization. These results confirm the advantage of incorporating spatial and textural constraints from multiple views and scenes, validating the robustness and adaptability of our environment-driven calibration strategy.

V. CONCLUSION

In this paper, we explore to extend a new definition called “environment-driven” for online LiDAR-camera extrinsic calibration. Unlike previous methods, our approach demonstrates human-like adaptability across diverse and complex environments. Inspired by human perceptual systems, we designed a scene discriminator that actively analyzes the calibration scenes from spatial and textural perspectives. By leveraging structural and textural consistency between LiDAR projections and camera images, our method achieves reliable 3D-2D correspondence matching, overcoming the challenge of cross-modal feature matching in sparse scenes encountered by earlier approaches. Additionally, we modeled the calibration process as a spatial-temporal joint optimization problem, achieving high-precision and robust extrinsic matrix estimation through multi-view optimization within individual scenes and joint optimization across multiple scenarios. Extensive experiments on real-world datasets demonstrate that our environment-driven calibration strategy achieves state-of-the-art performance.

REFERENCES

- [1] E. Arnold *et al.*, “A survey on 3D object detection methods for autonomous driving applications,” *IEEE Transactions on Intelligent Transportation Systems*, vol. 20, no. 10, pp. 3782–3795, 2019.
- [2] Y. Ai *et al.*, “LiDAR-camera fusion in perspective view for 3D object detection in surface mine,” *IEEE Transactions on Intelligent Vehicles*, 2023, DOI: 10.1109/TIV.2023.3343377.
- [3] C. Pelau, D.-C. Dabija, and I. Ene, “What makes an AI device human-like? the role of interaction quality, empathy and perceived psychological anthropomorphic characteristics in the acceptance of artificial intelligence in the service industry,” *Computers in Human Behavior*, vol. 122, p. 106855, 2021.
- [4] Y. Tian, Y. Chang, F. H. Arias, C. Nieto-Granda, J. P. How, and L. Carlone, “Kimera-multi: Robust, distributed, dense metric-semantic slam for multi-robot systems,” *IEEE Transactions on Robotics*, vol. 38, no. 4, 2022.
- [5] Z. Huang *et al.*, “Online, target-free lidar-camera extrinsic calibration via cross-modal mask matching,” *IEEE Transactions on Intelligent Vehicles*, pp. 1–12, 2024.
- [6] X. Liu, C. Yuan, and F. Zhang, “Targetless extrinsic calibration of multiple small fov lidars and cameras using adaptive voxelization,” *IEEE Transactions on Instrumentation and Measurement*, vol. 71, pp. 1–12, 2022.
- [7] Y. Li *et al.*, “DeepFusion: LiDAR-camera deep fusion for multi-modal 3D object detection,” in *Proceedings of the IEEE/CVF Conference on Computer Vision and Pattern Recognition (CVPR)*, 2022, pp. 17 182–17 191.
- [8] J. Cui *et al.*, “ACSC: Automatic calibration for non-repetitive scanning solid-state LiDAR and camera systems,” *arXiv preprint arXiv:2011.08516*, 2020.
- [9] G. Yan *et al.*, “Joint camera intrinsic and LiDAR-camera extrinsic calibration,” in *2023 IEEE International Conference on Robotics and Automation (ICRA)*. IEEE, 2023, pp. 11 446–11 452.
- [10] J. Beltrán *et al.*, “Automatic extrinsic calibration method for LiDAR and camera sensor setups,” *IEEE Transactions on Intelligent Transportation Systems*, vol. 23, no. 10, pp. 17 677–17 689, 2022.
- [11] G. Koo *et al.*, “Analytic plane covariances construction for precise planarity-based extrinsic calibration of camera and LiDAR,” in *2020 IEEE International Conference on Robotics and Automation (ICRA)*. IEEE, 2020, pp. 6042–6048.
- [12] Y. Xie *et al.*, “A4LidarTag: Depth-based fiducial marker for extrinsic calibration of solid-state LiDAR and camera,” *IEEE Robotics and Automation Letters*, vol. 7, no. 3, pp. 6487–6494, 2022.
- [13] D. Tsai *et al.*, “Optimising the selection of samples for robust LiDAR camera calibration,” in *2021 IEEE International Intelligent Transportation Systems Conference (ITSC)*. IEEE, 2021, pp. 2631–2638.
- [14] C. Yuan *et al.*, “Pixel-level extrinsic self calibration of high resolution LiDAR and camera in targetless environments,” *IEEE Robotics and Automation Letters*, vol. 6, no. 4, pp. 7517–7524, 2021.
- [15] G. Pandey *et al.*, “Automatic extrinsic calibration of vision and LiDAR by maximizing mutual information,” *Journal of Field Robotics*, vol. 32, no. 5, pp. 696–722, 2015.
- [16] T. Ma *et al.*, “CRLF: Automatic calibration and refinement based on line feature for LiDAR and camera in road scenes,” *arXiv preprint arXiv:2103.04558*, 2021.
- [17] J. Li *et al.*, “Automatic registration of panoramic image sequence and mobile laser scanning data using semantic features,” *ISPRS Journal of Photogrammetry and Remote Sensing*, vol. 136, pp. 41–57, 2018.
- [18] Y. Wang *et al.*, “Automatic registration of point cloud and panoramic images in urban scenes based on pole matching,” *International Journal of Applied Earth Observation and Geoinformation*, vol. 115, p. 103083, 2022.
- [19] Y. Han *et al.*, “Auto-calibration method using stop signs for urban autonomous driving applications,” in *2021 IEEE International Conference on Robotics and Automation (ICRA)*. IEEE, 2021, pp. 13 179–13 185.
- [20] J. Borer *et al.*, “From chaos to calibration: A geometric mutual information approach to target-free camera LiDAR extrinsic calibration,” in *Proceedings of the IEEE/CVF Winter Conference on Applications of Computer Vision (WACV)*, 2024, pp. 8409–8418.
- [21] X. Lv *et al.*, “LCCNet: LiDAR and camera self-calibration using cost volume network,” in *Proceedings of the IEEE/CVF Conference on*

- Computer Vision and Pattern Recognition (CVPR)*, 2021, pp. 2894–2901.
- [22] J. Shi *et al.*, “CalibRCNN: Calibrating camera and lidar by recurrent convolutional neural network and geometric constraints,” in *2020 IEEE/RSJ International Conference on Intelligent Robots and Systems (IROS)*. IEEE, 2020, pp. 10 197–10 202.
 - [23] G. Zhao *et al.*, “CalibDNN: multimodal sensor calibration for perception using deep neural networks,” in *Signal Processing, Sensor/Information Fusion, and Target Recognition XXX*, vol. 11756. SPIE, 2021, pp. 324–335.
 - [24] G. Iyer *et al.*, “CalibNet: Geometrically supervised extrinsic calibration using 3D spatial transformer networks,” in *2018 IEEE/RSJ International Conference on Intelligent Robots and Systems (IROS)*. IEEE, 2018, pp. 1110–1117.
 - [25] K. Yuan *et al.*, “RGGNet: Tolerance aware LiDAR-camera online calibration with geometric deep learning and generative model,” *IEEE Robotics and Automation Letters*, vol. 5, no. 4, pp. 6956–6963, 2020.
 - [26] A. Geiger *et al.*, “Are we ready for autonomous driving? the KITTI vision benchmark suite,” in *2012 IEEE conference on Computer Vision and Pattern Recognition (CVPR)*. IEEE, 2012, pp. 3354–3361.
 - [27] K. Koide *et al.*, “General, single-shot, target-less, and automatic LiDAR-camera extrinsic calibration toolbox,” in *2023 IEEE International Conference on Robotics and Automation (ICRA)*, 2023, pp. 11 301–11 307.
 - [28] M. A. Goodale and A. D. Milner, “Separate visual pathways for perception and action,” *Trends in Neurosciences*, vol. 15, no. 1, pp. 20–25, 1992.
 - [29] N. Ou *et al.*, “Targetless extrinsic calibration of camera and low-resolution 3D LiDAR,” *IEEE Sensors Journal*, 2023.
 - [30] Y. Liao *et al.*, “SE-Calib: Semantic edges based LiDAR-camera bore-sight online calibration in urban scenes,” *IEEE Transactions on Geoscience and Remote Sensing*, 2023, DOI: 10.1109/TGRS.2023.3278024.
 - [31] F. Lv and K. Ren, “Automatic registration of airborne LiDAR point cloud data and optical imagery depth map based on line and points features,” *Infrared Physics & Technology*, vol. 71, pp. 457–463, 2015.
 - [32] J. Castorena *et al.*, “Autocalibration of LiDAR and optical cameras via edge alignment,” in *2016 IEEE International Conference on Acoustics, Speech and Signal Processing (ICASSP)*. IEEE, 2016, pp. 2862–2866.
 - [33] S. Tang *et al.*, “Robust calibration of vehicle solid-state LiDAR-camera perception system using line-weighted correspondences in natural environments,” *IEEE Transactions on Intelligent Transportation Systems*, 2023, DOI: 10.1109/TITS.2023.3328062.
 - [34] B. Zhang and R. T. Rajan, “Multi-FEAT: Multi-feature edge alignment for targetless camera-LiDAR calibration,” *arXiv preprint arXiv:2207.07228*, 2022.
 - [35] D. Zhang *et al.*, “An overlap-free calibration method for LiDAR-camera platforms based on environmental perception,” *IEEE Transactions on Instrumentation and Measurement*, vol. 72, pp. 1–7, 2023.
 - [36] J. Yin *et al.*, “Automatic and targetless LiDAR-camera extrinsic calibration using edge alignment,” *IEEE Sensors Journal*, 2023.
 - [37] N. Ou *et al.*, “Targetless LiDAR-camera calibration via cross-modality structure consistency,” *IEEE Transactions on Intelligent Vehicles*, 2023, DOI: 10.1109/TIV.2023.3337490.
 - [38] Y. Zhu *et al.*, “Online camera-LiDAR calibration with sensor semantic information,” in *2020 IEEE International Conference on Robotics and Automation (ICRA)*. IEEE, 2020, pp. 4970–4976.
 - [39] P.-E. Sarlin *et al.*, “SuperGlue: Learning feature matching with graph neural networks,” in *Proceedings of the IEEE/CVF Conference on Computer Vision and Pattern Recognition (CVPR)*, 2020, pp. 4938–4947.
 - [40] L. Yang *et al.*, “Depth Anything V2,” *arXiv:2406.09414*, 2024.
 - [41] Kirillov *et al.*, “Segment Anything,” in *Proceedings of the IEEE/CVF International Conference on Computer Vision (CVPR)*, 2023, pp. 4015–4026.
 - [42] N. Schneider *et al.*, “RegNet: Multimodal sensor registration using deep neural networks,” in *2017 IEEE Intelligent Vehicles Symposium (IV)*. IEEE, 2017, pp. 1803–1810.

Environment-Driven Online LiDAR-Camera Extrinsic Calibration

Supplementary Material

VI. DETAILS OF THE ALGORITHM IMPLEMENTATION

As presented in the ‘‘Dual-Path Correspondence Matching’’ in Sect. III-B, we initially adopted the method described in [5] for cross-modal mask matching. [5] proved that when two 3D LiDAR points q^V (reference) and p^V (target) in the virtual camera coordinate system are close in depth, the relationship of their projection coordinates $\tilde{p}_{v,c}$ on virtual image and camera image can be written by follows:

$$\tilde{p}_c \approx A\tilde{p}_v + b. \quad (11)$$

In practice, we use the following affine transformation:

$$\begin{pmatrix} \tilde{p}_c & \tilde{q}_c \end{pmatrix} = \begin{pmatrix} sR^A & t^A \\ \mathbf{0}^\top & 1 \end{pmatrix} \begin{pmatrix} \tilde{p}_v & \tilde{q}_v \end{pmatrix} \quad (12)$$

to represent this affine transformation (mentioned in Sect. III-B), where $R^A \in SO(2)$ represents the rotation matrix, t^A denotes the translation vector, and s represents the scaling factor. We can assume that after the affine transformation, any points within a given mask in the LIP image perfectly align with the corresponding points from the RGB image, and thus:

$$\begin{aligned} \hat{c}^V &= sR^A c^V + t^A, \\ \hat{o}^V &= sR^A o^V + t^A. \end{aligned} \quad (13)$$

where \hat{o}^V and \hat{c}^V represent the updated coordinates of the instance’s center and corner points in the virtual image, respectively. In this case, R^A can be obtained using the following expression:

$$R^A = \begin{pmatrix} \cos \theta & -\sin \theta \\ \sin \theta & \cos \theta \end{pmatrix}, \quad (14)$$

where

$$\theta = \frac{1}{N} \sum_{i=1}^N \left(\arctan \frac{\mathbf{1}_y^\top (c_i^V - o^V)}{\mathbf{1}_x^\top (c_i^V - o^V)} - \arctan \frac{\mathbf{1}_y^\top (c_i^C - o^C)}{\mathbf{1}_x^\top (c_i^C - o^C)} \right) \quad (15)$$

is the angle between the vectors originating from the mask centers and pointing to their respective matched corner points. s can then be expressed as follows:

$$s = \frac{w^C h^C}{w^V h^V}, \quad (16)$$

which represents the ratio between the areas of the bounding boxes associated with the RGB image and the LIP image. Finally, according to (13), t^A can be obtained as follows:

$$t^A = o^C - sR^A o^V. \quad (17)$$

In DPCM, we utilize the affine transformation estimated by (14)-(17) as a semantic prior to guide the dense correspondence matching between LiDAR and camera.

Additionally, the component $H(e_{i,k}^V, e_{j,k}^C)$ of the structural consistency mentioned in Sect. III-B is defined as follows:

$$H(e_{i,k}^V, e_{j,k}^C) = \frac{\| (e_{i,k}^V - \hat{c}_i^V) - (e_{j,k}^C - c_j^C) \|_2}{\| e_{i,k}^V - \hat{c}_i^V \|_2 + \| e_{j,k}^C - c_j^C \|_2}, \quad (18)$$

Algorithm 1 Dual-Path Correspondence Matching

Require:

Spatial pathway: Masks (including detected corner points) obtained from the LIP and RGB image.

Textural pathway: Masks (including detected corner points) obtained from the LDP and depth images.

Stage 1 (Reliable mask matching):

(1) Conduct cross-modal mask matching by adopting the method described in [5].

(2) Estimate sR^A and t^A using (14)-(17).

Stage 2 (Dense correspondence matching):

(1) For each pathway, update all masks in the virtual image using sR^A and t^A .

(2) Construct the corner point cost matrix M^C using (6). (3) Select matches with the lowest costs in both horizontal and vertical directions of $M^C(x)$ as the optimum correspondence matches.

(4) Aggregate all corner point correspondences to form the sets $\mathcal{C} = \{(p_i^L, p_i) \mid i = 1, \dots, q\}$.

which represents the similarity of the neighboring vertices between the current and target corner points.

The pseudo code of DPCM is shown in Algorithm 1. Thanks to the generalizable discriminator, the multiple views generated by the virtual cameras provide comprehensive spatial and textural cues to formulate the feature matching to a 3D-2D correspondence matching process. The entire DPCM is efficient because it primarily focuses on 2D structural and textural consistency computation, rather than complex 3D point cloud registration.

For the spatial-temporal relative pose optimization, as presented in Sect. III-C, we utilize a Gaussian kernel $\mathcal{K}(d'_j, \bar{d}')$ to calculate the depth-normalized reprojection error. In detail, $\mathcal{K}(d'_j, \bar{d}')$ is defined as follows:

$$\mathcal{K}(d'_j, \bar{d}') = \exp\left(\frac{-\|d'_j - \bar{d}'\|^2}{2\bar{d}_g^2}\right), \quad (19)$$

where \bar{d}_g is the true average depth of the correspondences.

In our algorithm implementation, we use the pinhole model as the projection model to calculate the reprojection error presented in (7) and (10). When the camera intrinsic matrix \mathbf{K} is known, the 3D LiDAR point $p^L = [x^L, y^L, z^L]^\top$ can be projected onto a 2D image pixel $p = [u, v]^\top$ using the following expression:

$$\pi(p^L) = \tilde{p} = \frac{\mathbf{K}p^L}{(p^L)^\top \mathbf{1}_z}, \quad (20)$$

where \tilde{p} represents the homogeneous coordinates of p and $\mathbf{1}_z = [0, 0, 1]^\top$. Given the extrinsic transformation ${}^C_L T$, the



Fig. 7. An example of the data fusion result on KITTI odometry using our calibration parameters.

reprojection between the correspondence $(\mathbf{p}_i^L, \mathbf{p}_i)$ can be obtained as follows:

$$\epsilon_i = \left\| \pi(\mathcal{C}_L^T \mathbf{R} \mathbf{p}_i^L) - \tilde{\mathbf{p}}_i \right\|_2 = \left\| \frac{\mathbf{K}(\mathcal{C}_L^T \mathbf{R} \mathbf{p}_i^L + \mathcal{C}_L^T \mathbf{t})}{(\mathcal{C}_L^T \mathbf{R} \mathbf{p}_i^L + \mathcal{C}_L^T \mathbf{t})^\top \mathbf{1}_z} - \tilde{\mathbf{p}}_i \right\|_2. \quad (21)$$

By applying the Gaussian normalization G given in (8), the reprojection errors of different correspondences are provided with weights based on the depth distribution.

VII. CALIBRATION PARAMETERS

To foster future research toward LiDAR-camera sensor fusion, we release the calibration parameters that we obtained with our method for the 00 sequence of the KITTI odometry. In detail, we provide the rotation matrices and translation vectors for projecting the LiDAR point cloud into the camera image or rendering LiDAR point clouds with colors.

Calibration Parameters for Left RGB Camera

$$\mathbf{R} = \begin{bmatrix} -2.5805e-04 & -9.9997e-01 & -7.5245e-03 \\ -6.8854e-03 & 7.5261e-03 & -9.9995e-01 \\ 9.9998e-01 & -2.0623e-04 & -6.8872e-03 \end{bmatrix}$$

$$\mathbf{t} = [0.070478 \quad -0.057913 \quad -0.286353]^\top$$

Calibration Parameters for Right RGB Camera

$$\mathbf{R} = \begin{bmatrix} -5.3850e-04 & -9.9998e-01 & -6.6623e-03 \\ -8.1213e-03 & 6.6665e-03 & -9.9994e-01 \\ 9.9997e-01 & -4.8437e-04 & -8.1247e-03 \end{bmatrix}$$

$$\mathbf{t} = [-0.494557 \quad -0.042731 \quad -0.261487]^\top$$

An example of the data fusion result using our extrinsic calibration parameters for the left camera in KITTI odometry is shown in Fig. 7.

VIII. DETAILS OF EXPERIMENTAL CONFIGURATION

A. Datasets

We have conducted extensive experiments on KITTI odometry and MIAS-LCEC (including MIAS-LCEC-TF70 and MIAS-LCEC-TF360) datasets. Now we provide their details:

TABLE VI
DATASET STATISTICS OF KITTI ODOMETRY 00-09 SEQUENCES.

	00	01	02	03	04	05	06	07	08	09
Initial Pairs	4541	1101	4661	801	271	2761	1101	1101	4071	4091
Downsampling	10	10	10	10	2	10	10	10	10	410
Evaluated Pairs	455	111	467	81	136	277	111	111	408	410

- **KITTI odometry:** KITTI odometry is a large-scale public dataset recorded using a vehicle equipped with two RGB cameras Point Grey Flea 2 and one LiDAR of type Velodyne HDL-64E. Sensor data is captured at 10 Hz. We utilize the first 10 sequences (00-09) for evaluation.
- **MIAS-LCEC-TF70:** MIAS-LCEC-TF70 is a diverse and challenging dataset that contains 60 pairs of 4D point clouds (including spatial coordinates with intensity data) and RGB images, collected using a Livox Mid-70 LiDAR and a MindVision SUA202GC camera, from a variety of indoor and outdoor environments, under various scenarios as well as different weather and illumination conditions. This dataset is divided into six subsets: residential community, urban freeway, building, challenging weather, indoor, and challenging illumination, to comprehensively evaluate the algorithm performance.
- **MIAS-LCEC-TF360:** MIAS-LCEC-TF360 contains 12 pairs of 4D point clouds and RGB images, collected using a Livox Mid-360 LiDAR and a MindVision SUA202GC camera from both indoor and outdoor environments. Since the Livox Mid-360 LiDAR has a scanning range of 360° , it produces a sparser point cloud compared to that generated by the Livox Mid-70 LiDAR. Additionally, the significant difference in the FoV between this type of LiDAR and the camera results in only a small overlap in the collected data. Consequently, this dataset is particularly well-suited for evaluating the adaptability of algorithms to challenging scenarios

B. Metrics

As stated in Sect. IV-A, to comprehensively evaluate the performance of LCEC approaches, we use the magnitude e_r of

TABLE VII
DETAILS OF COMPARISON METHODS.

Methods	Publication	Type	Parameterization or Basic Tools	Computation Speed	Accuracy	Provide Code?
UMich [15]	JFR 2015	MI-based	Mutual Information	Medium	Medium	Yes
RegNet [42]	IV 2017	Learning-based	CNN	Medium	Medium	No
CalibNet [24]	IROS 2018	Learning-based	Geometrically Supervised Deep Learning Network	High	Low	Yes
RGNet [25]	RAL 2020	Learning-based	Deep Learning Network, Riemannian Geometry	High	Medium	Yes
CalibRCNN [22]	IROS 2020	Learning-based	RCNN	Medium	Medium	No
CalibDNN [23]	SPIE 2021	Learning-based	Deep Learning Network	Medium	Medium	No
LCCNet [21]	CVPR 2021	Learning-based	CNN, L1-Loss	High	Medium	Yes
HKU-Mars [14]	RAL 2021	Edge-based	Adaptive Voxel	Low	Very Low	Yes
CRLF [16]	arXiv 2021	Semantic-based	Segmented Road Pole and Lane, Perspective-3-Lines	Low	Low	Yes
DVL [27]	ICRA 2023	Point-based	SuperGlue, RANSAC, Normalized Information Distance	Medium	High	Yes
Borer <i>et al.</i> [20]	WACV 2024	Learning-based	CNN, Geometric Mutual Information	High	High	No
MIAS-LCEC [5]	T-IV 2024	Semantic-based	MobileSAM, C3M, PnP	Low	High	Yes

Euler angle error and the magnitude e_t of the translation error to quantify the calibration errors. Here, we give the specific calculation formula of e_r and e_t ³:

$$\begin{aligned} e_r &= \left\| {}^C_L \mathbf{r}^* - {}^C_L \mathbf{r} \right\|_2, \\ e_t &= \left\| -({}^C_L \mathbf{R}^*)^{-1} {}^C_L \mathbf{t}^* + {}^C_L \mathbf{R}^{-1} {}^C_L \mathbf{t} \right\|_2, \end{aligned} \quad (22)$$

where ${}^C_L \mathbf{r}^*$ and ${}^C_L \mathbf{r}$ represent the estimated and ground-truth Euler angle vectors, computed from the rotation matrices ${}^C_L \mathbf{R}^*$ and ${}^C_L \mathbf{R}$, respectively. Similarly, ${}^C_L \mathbf{t}^*$ and ${}^C_L \mathbf{t}$ denote the estimated and ground-truth translation vectors from LiDAR to camera, respectively.

C. Data Preparation

The dataset statistics of KITTI odometry are presented in Table VI. It can be observed that there are a total of 24500 pairs of point clouds and images in KITTI odometry. Note that most of the SoTA comparison methods are slow to complete calibration with a single frame. For the comparison algorithms that provided source code, we performed calibration every ten frames (except for 2 frames in 04 sequence), enhancing the efficiency of the experiments without compromising the validity of the evaluation.

D. Details of Comparison Methods

The details of the comparison methods are illustrated in Table VII. For algorithms that did not release their code, we directly reference the results published in their papers. Notably, RegNet [42], Borer *et al.* [20], and CalibDNN [23] employ different experimental datasets and evaluation processes, which limits the potential for a fully quantitative comparison. Furthermore, these methods do not specify which frames from the KITTI dataset were used for training and testing. Therefore, we rely on the published results to compare these approaches to others on the KITTI odometry 00 sequence.

IX. ADDITIONAL EXPERIMENTS

A. Comparison of Correspondence Matching

We present a comparison of correspondence matching results in Fig. 8. The visualized results indicate that our method

³The translation from LiDAR pose to camera pose is $-{}^C_L \mathbf{R}^{-1} {}^C_L \mathbf{t}$ when (1) is used to depict the point translation.

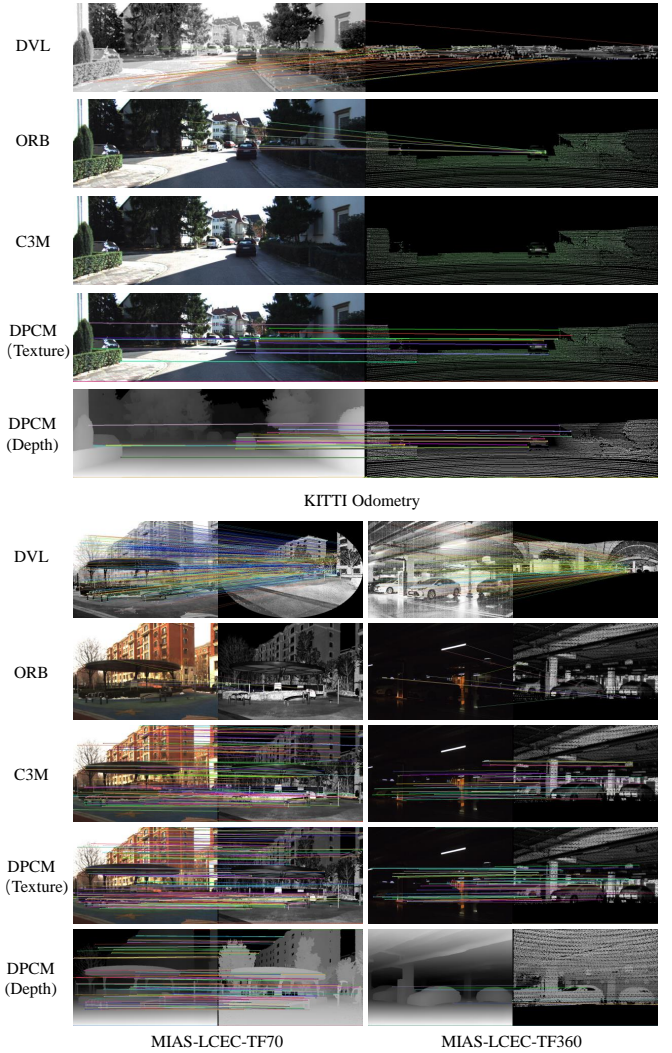


Fig. 8. Qualitative comparisons of correspondence matching.

significantly outperforms other correspondence matching algorithms employed in the comparison calibration methods. Specifically, our approach yields substantially more correct correspondences than ORB, DVL (which employs SuperGlue for direct 3D-2D correspondence matching), and C3M (the cross-modal mask matching algorithm provided by MIAS-LCEC). This demonstrates the superior adaptability of DPCM, particularly in scenarios involving sparse point clouds with minimal geometric and textural information.

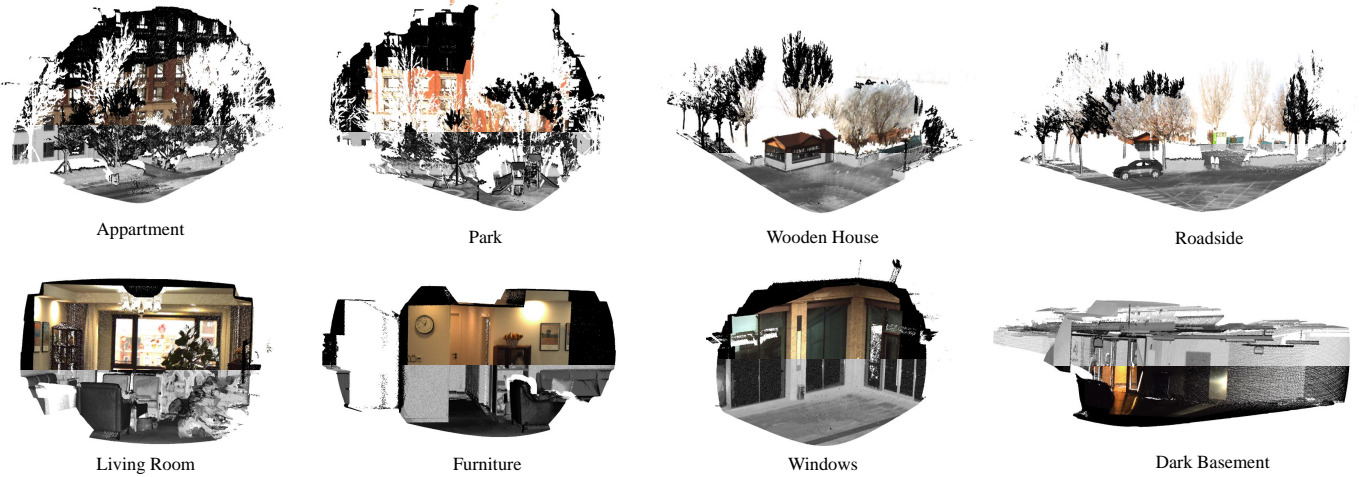


Fig. 9. Visualization of EdO-LCEC calibration results through LiDAR and camera data fusion on MIAS-LCEC datasets.

The ORB algorithm relies on the fast Harris corner detector for keypoint extraction and employs a binary descriptor for efficient matching based on Hamming distance. While ORB performs well in image-to-image matching, it struggles with cross-modal feature matching, especially in LiDAR-camera integration scenarios. Conversely, while DVL and C3M perform adequately on dense point clouds such as those in the MIAS-LCEC-TF70, they face significant challenges when applied to the sparse point clouds in the KITTI odometry and MIAS-LCEC-TF360. The narrow overlapping field of view between LiDAR and camera in KITTI odometry creates difficulties in identifying reliable correspondences, particularly along the edges of the LiDAR field of view. This limitation significantly reduces the matching accuracy of DVL. Similarly, C3M, which restricts matching to corner points within aligned masks, struggles with sparse point clouds and limited sensor overlap.

Our proposed DPCM resolves these issues by incorporating both spatial and textural constraints. Unlike C3M, which treats mask instance matching as a strict constraint, DPCM uses it as a prior, enabling the generation of denser 3D-2D correspondences. This refinement significantly enhances the robustness of the algorithm in sparse environments and restricted fields of view, ensuring reliable calibration even under challenging conditions.

B. More Visualization Results

In this section, we provide more detailed visualization results of EdO-LCEC through LiDAR and camera data fusion on MIAS-LCEC datasets. Fig. 9 demonstrate that LiDAR point cloud and camera image aligned almost perfectly along the textural and geometric edges, proving the accuracy of our calibration results. It can also be observed that our method performs well in challenging conditions, particularly under poor illumination and adverse weather, or when few geometric features are detectable. This impressive data fusion result further validates the critical role of LiDAR-camera extrinsic calibration. The seamless integration of spatial and textural modalities equips robots with a human-like perceptual

ability to interpret and interact with their surroundings. Our environment-driven approach bridges the gap toward the flexible and adaptive machines often envisioned in science fiction.